

EVOLUTIONARY MODELS OF ROTATING
LOW MASS STARS:
Effects of internal magnetic fields

Maarten Pieter Leo Suijs

June 16, 2006

This is the final thesis that concludes the 5 year curriculum of the specialization Astronomy at the Faculty of Physics and Astronomy, Utrecht University.

Supervisor: Prof. dr. Norbert Langer



Universiteit Utrecht

The work described in this thesis was carried out at the Astronomical Institute, Utrecht University, The Netherlands.

Abstract

In order to study the influence of magnetic fields on the angular momentum evolution and on rotationally induced mixing during the thermally pulsing phase of stars with $M_{\star} = 1.0 \dots 3.0 M_{\odot}$, I have calculated stellar evolution models with initial masses 1.0, 1.5, 2.0, and $3.0 M_{\odot}$, $Z = 0.02$, and initial velocities of 2&10, 45, 140, and 250 km s^{-1} . Calculations were performed with a stellar evolution code that can handle differential rotation, can include magnetic fields according to the Spruit-dynamo principle (Spruit 2002) and that has an extensive nuclear network. Models were calculated with and without magnetic fields. Calculations are pursued from zero-age main sequence through at least four thermal pulses on the asymptotic giant branch.

I found that the total angular momentum in the cores of all models remained constant after core helium ignition (or earlier). I also found that after core helium ignition, my magnetic model $1.0 M_{\odot}$ model with an initial velocity of 2 km/s had a factor ~ 2 less total angular momentum in the core than its non-magnetic counterpart. The other magnetic models ended up with factors $\sim 7 \dots \sim 30$ less total angular momentum in their cores than their non-magnetic counterparts.

Assuming the total core angular momentum does not change anymore during the evolution from the asymptotic giant branch to the white dwarf stage, I predicted white dwarf rigid rotation rates using the principle of gyration radii. All non-magnetic models, except for the slow $1.0 M_{\odot}$ model, produced white dwarfs with rotation rates well above the observational upper limit by Berger et al. (2005). All magnetic models produced white dwarfs below this upper limit. This result is similar to results from Heger et al. (2005), since observational data for neutron stars favoured their magnetic models as well.

From this, I conclude that magnetic fields are essential to understand the angular momentum evolution of stars of all masses.

I also studied the influence of magnetic fields on the diffusion coefficients of rotationally induced instabilities in the areas where the s-process is expected to take place in stars of these masses. I found that magnetic fields bring the diffusion coefficients down by factors of $10^2 \dots 10^3$, except in the case of the $1.0 M_{\odot}$ model with an initial velocity of 2 km/s.

I was not able to produce models with a deep enough third dredge-up to investigate if these lower diffusion coefficients are able to maintain a ^{13}C -pocket next to a ^{14}N -pocket without fully mixing the two. The reduction of the diffusion coefficients is promising, however, since Herwig et al. (2003) showed that a reduction by a factor of 10^2 is enough to produce a ^{13}C -pocket next to a ^{14}N -pocket in their $3.0 M_{\odot}$ models.

I conclude that magnetic fields can reduce the diffusion coefficients in models

of $1.5 \dots 3.0 M_{\odot}$ to such an extent that, with a stronger third dredge-up, these models could produce a suitable s-process environment.

Contents

1	Introduction	7
1.1	Rotation in low mass stars	7
1.1.1	Evolution and rotation	7
1.1.2	Previous studies	8
1.2	Nucleosynthesis in low mass stars: s-process	8
1.2.1	The s-process	8
1.2.2	Previous studies	11
2	Method	13
2.1	Description of our stellar evolution code	13
2.2	Initial models	14
3	Angular momentum evolution and white dwarf spins	15
3.1	Pre-helium flash	15
3.2	From helium flash through AGB/thermally pulsing AGB	22
3.3	White dwarf spins	24
4	Chemical mixing	29
4.1	Early evolutionary phases	29
4.2	AGB/TP-AGB phase	29
5	Summary and outlook	37
6	Appendix	39
6.1	What are thermal pulses and the third dredge up?	39
6.2	Hertzprung-Russel diagram	40

Chapter 1

Introduction

1.1 Rotation in low mass stars

1.1.1 Evolution and rotation

Observations (see Fig. 1.1) tell us that low mass stars¹ start out as very rapid rotators. They have zero-age main sequence surface velocities up to the order of 10^2 km/s. Stars with masses around $1.2 M_{\odot}$ and lower slow down quickly during the main sequence evolution due to magnetic braking (for details, see for example Stępień 1988), while stars with higher masses remain rapid rotators during the main sequence evolution.

At the end of the main sequence evolution, a hydrogen burning shell is formed, and these stars become red giants: their envelopes will expand and spin down and their cores will contract and spin up. When stars with masses $\lesssim 2 M_{\odot}$ have reached a core density of $\sim 10^6$ g/cm³, they ignite their degenerate helium core violently (core helium flash) and undergo a phase of core helium burning. Stars with masses $\gtrsim 2 M_{\odot}$ ignite the helium core in a non-explosive way, because it is non-degenerate. When the central helium becomes exhausted, a helium burning shell is formed and the stars move up the asymptotic giant branch (AGB) in the Hertzsprung-Russel diagram (see Fig. 1.2). On the AGB, the helium shell becomes unstable and gives rise to thermal pulses (see Appendix) during which the stars will move up and down the AGB. During and after this ‘thermally pulsing AGB phase’, the stellar winds blow away the envelopes and the CO-cores remain. The stars have become white dwarfs and will only cool down (see Fig. 1.2).

If one estimates the white dwarf total angular momentum from stellar models without any angular momentum transport mechanisms (able to transport angular momentum through different mass shells) by using the initial-final mass relation for white dwarfs (for example Weidemann 2000), one finds that the white dwarfs from progenitors without magnetic braking contain a factor $\gtrsim 10$ too much angular momentum than observations tell us.

This means that there must be at least one mechanism that transports angular momentum out of the stellar cores somewhere during their evolution. Since these stars have a slow rotating envelope touching a fast rotating core, we

¹Normally, when astronomers talk about ‘low mass stars’ they refer to stars with masses below $2 M_{\odot}$. In this thesis ‘low mass’ refers to the mass range of $1.0 \dots 3.0 M_{\odot}$.

know that there must be angular velocity gradients in these stars: the stars rotate differentially. Differential rotation gives rise to rotational instabilities that can transport matter, but also angular momentum. Since differential rotation means that there are charged particles that move with different velocities, differential rotation also results in internal magnetic fields. Magnetic effects can also transport matter and angular momentum.

1.1.2 Previous studies

The first models of this type were calculated by Langer et al. (1999) for the purpose of studying the various rotationally induced mixing processes and nucleosynthesis during the thermally pulsing AGB phase (see Appendix). Studies by Heger et al. (2000) have resulted in realistic values for the efficiency of various rotationally induced instabilities. Siess et al. (2004) have calculated the most recent detailed evolutionary models of rotating low mass stars. Here, the focus was s-process nucleosynthesis as well. Palacios et al. (2003) showed that mean molecular weight barriers constrain the rotational profile of low-mass stars.

Talon & Charbonnel (2005) showed that gravitational waves influence the rotational profile and reduce the amount of rotational mixing in a $1.2 M_{\odot}$ model. Our code, however, can not handle gravitational waves. Eggenberger et al. (2005) showed that magnetic fields can reproduce the solar rotation profile in their $1.0 M_{\odot}$ models. This means that gravitational waves and magnetic fields are both promising candidates for angular momentum transport.

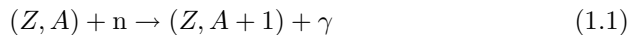
To study the transport of angular momentum throughout the evolution of low mass stars, I have computed rotating stellar models including the effects of rotational instabilities only and including the effects of rotational instabilities *plus* the effects of internal magnetic fields. I compared the angular momentum evolution of these two cases. I also estimated white dwarf rotational velocities from my results and compared them to a recently found observational upper limit by Berger et al. (2005). The method used to produce my models and a description of the initial models is can be found in Chap. 2. The results of this investigation can be found in Chap. 3. Chap. 4 shows the results of my study on chemical mixing, described in Sect. 1.2. My conclusions are presented in Chap. 5.

1.2 Nucleosynthesis in low mass stars: s-process

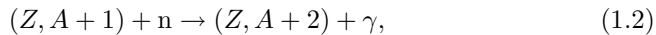
1.2.1 The s-process

The s-process is a nucleosynthesis process in which nuclei heavier than ^{56}Fe are formed through neutron capture on ^{56}Fe (and heavier) nuclei. For heavy elements with mass number A and proton number Z , we have the following options to climb in mass number and proton number through neutron capture and β^{-} -decay:

The heavy element captures a neutron through



If $(Z, A + 1)$ is a stable isotope, it can capture another neutron through



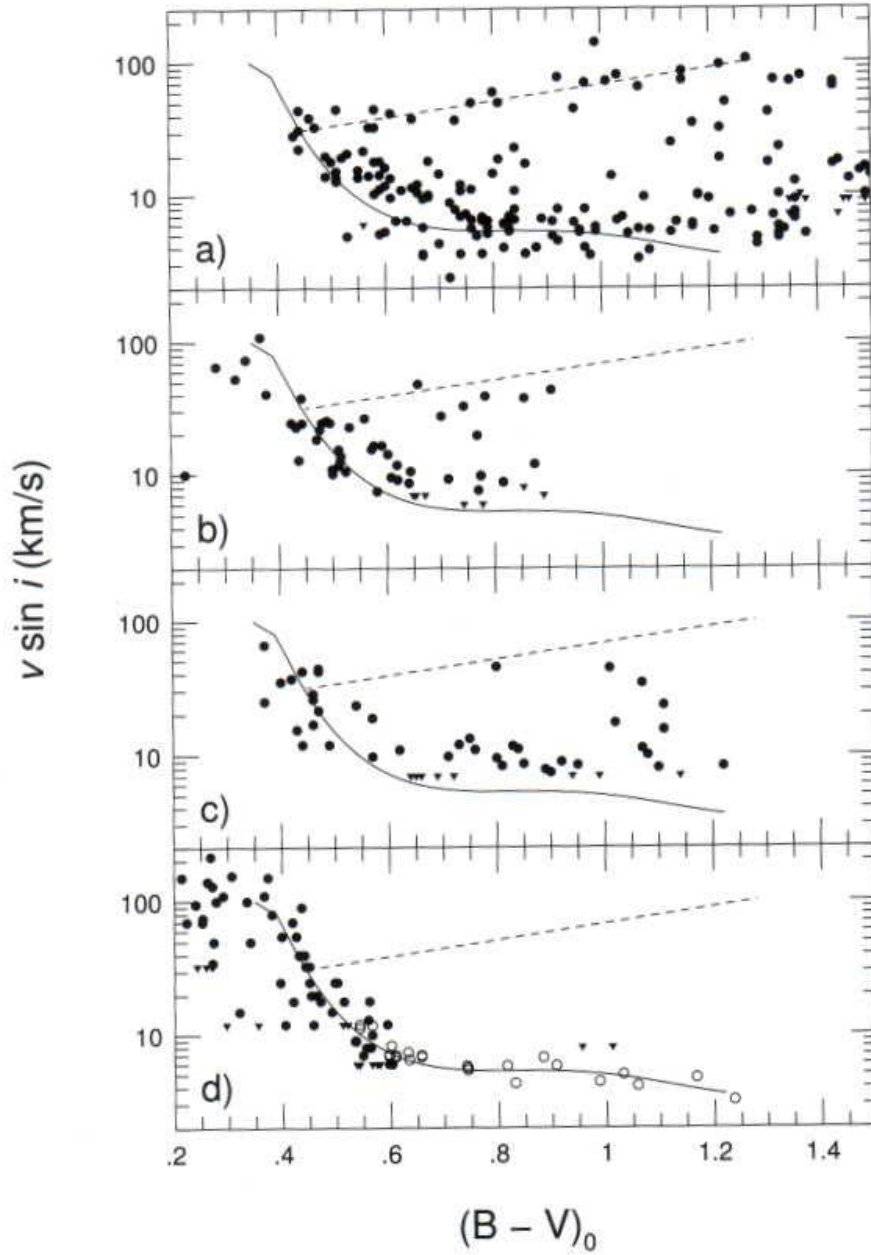


Figure 1.1: $(B-V)_0$ versus rotational velocities for four clusters: a) Pleiades (age ~ 100 Myr), b) NGC2516 (age ~ 200 Myr), c) M34 (age ~ 200 Myr) and d) Hyades (age ~ 600 Myr). The sun has $(B-V)_0 \approx 0.7$. We see that stars with $(B-V)_0 \gtrsim 0.6$ all slow down in the early stage of the main sequence (due to magnetic braking). Stars with $(B-V)_0 \lesssim 0.6$ remain rapid rotators. Image from Stauffer (2003).

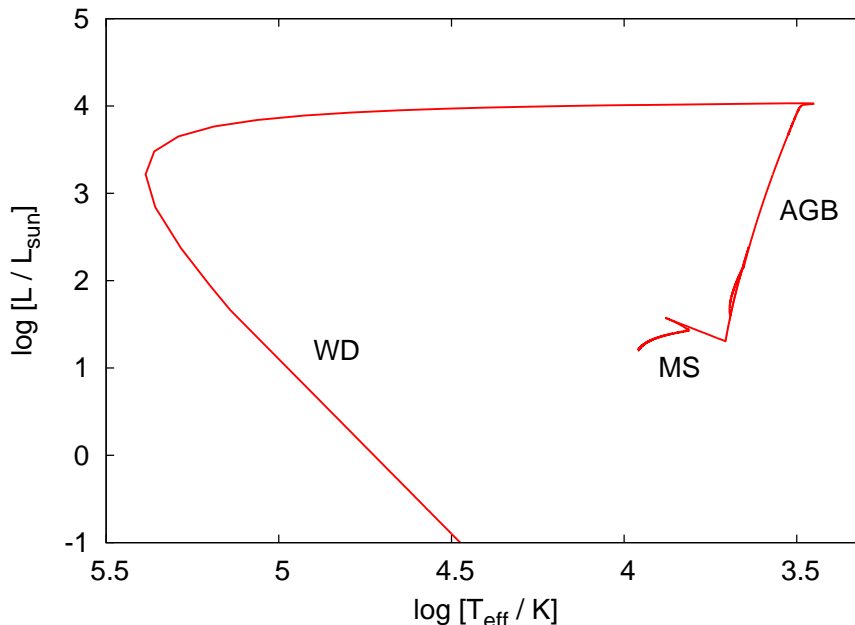
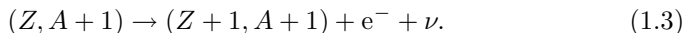


Figure 1.2: Evolution of a $2 M_{\odot}$ star in the Hertzsprung-Russell diagram, from main sequence (MS), via the asymptotic giant branch (AGB) to the white dwarf stage (WD). Data courtesy of Rob Izzard.

but if $(Z, A + 1)$ is β^- unstable, it will decay before another neutron is captured through

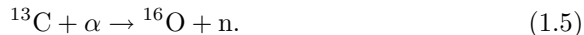


In this way, increasingly heavy elements (and their different isotopes) can be formed.

For the s-process to take place, we need heavy elements and we need free neutrons. Heavy elements are available (although sometimes in tiny abundances) in every non-primordial star. Free neutrons however, are not. There are only two efficient neutron sources in hydrostatic stellar evolution:



and



The first reaction takes place during the late helium burning of massive stars ($M_{\star} \gtrsim 8 M_{\odot}$) at temperatures around $5 \cdot 10^8 \text{K}$, which is the perfect environment for the weak s-process component. The second reaction takes place in stars with masses $\lesssim 8 M_{\odot}$ on the asymptotic giant branch (AGB) during the evolutionary phase in which the helium burning shell is unstable and gives rise to thermal pulses and the third dredge-up (an explanation of thermal pulses and third dredge-up can be found in Sect. 6.1 of the Appendix). In this so-called thermally pulsing AGB phase, the convective helium shell flash brings up ${}^{12}\text{C}$, the third dredge-up (3DU) brings down hydrogen (= protons) and if the 3DU is strong

enough to penetrate deeper than the position of the hydrogen shell before the helium flash, this proton-rich layer will touch the carbon-rich layer.

The so called neutron ‘donor’ ^{13}C needed for Eq. 1.5 can be formed through:



If there are enough protons available, ^{13}C can capture another proton and form ^{14}N through:



So, to produce ^{13}C , we need the neighbouring ^{12}C -layer and proton-layer to mix. A candidate to accomplish this is rotational mixing (see Sect. 1.2.2).

The above is not only theory: we know that the third dredge-up takes place in AGB stars, because of the existence of so-called ‘carbon stars’. These are stars with an extremely high ^{12}C -abundance in the envelopes. This means that the convective envelope must have reached down to the carbon core of these stars numerous times: the third dredge-up exists. For a more detailed description of carbon stars, see for example Abia et al. (2003). We also know that the s-process takes place in these stars, since there are observations of ^{99}Tc (technetium) lines in AGB stars (see for example Lambert 1989). ^{99}Tc has a half-life time of about 10^5 years (\ll the lifetime of AGB stars). This means that the ^{99}Tc in these stars could not have been there from birth, so it was formed inside the stars. Since ^{99}Tc is an element that can only be formed through the s-process, we know that the s-process must happen in AGB stars.

1.2.2 Previous studies

Generally, stellar evolution models do not form any ^{13}C during the thermally pulsing AGB phase. Langer et al. (1999) showed that rotationally induced mixing, however, *can* mix ^{12}C and protons to form ^{13}C . Herwig et al. (2003) and Siess et al. (2004) found that realistic values for rotational mixing from Heger et al. (2000) provide enough rotationally induced chemical mixing during the interpulse phase to mix protons with ^{12}C to form a layer of ^{13}C (the ^{13}C -pocket), but they found that the mixing was so strong that the ^{14}N that was formed mixed all over the ^{13}C -pocket. This is problematic, since ^{14}N acts as a neutron ‘poison’. ^{14}N captures free neutrons very efficiently through the following reaction:



If all the ^{13}C is mixed with ^{14}N , neutrons from Eq. 1.5 will be captured by ^{14}N before they can be a part of the s-process. Herwig et al. (2003) also showed that a reduction of the rotationally induced diffusion coefficients with a factor of 10^2 would still produce a ^{13}C -pocket, but would prevent ^{14}N to mix all over it. Since we know from Heger et al. (2000) what the efficiency of rotational mixing effects should be, we have to look for an extra mechanism that could bring the diffusion coefficients down.

Magnetic fields have been suggested as a solution for this problem (Herwig 2005). We expect magnetic fields to keep stellar models rotating more towards rigid rotation through the transport of angular momentum which will decrease the angular velocity gradients and therefore also the rotationally induced mixing.

I have investigated if magnetic fields reduce the amount of rotational mixing during the interpulse phase of low mass stellar models significantly to create a suitable s-process environment. The results of this investigation are presented in Chap. 4. The method used to produce my stellar models is described in Chap. 2. I summarize and provide an outlook on future research in Chap. 5.

Chapter 2

Method

2.1 Description of our stellar evolution code

We performed stellar evolution calculations using a 1-dimensional hydrodynamic stellar evolution code (Petrovic et al. 2005 and references therein). This code solves the basic equations for stellar evolution (continuity equation, equation of motion, conservation of energy/mass, radiative/convective energy transport, diffusive/convective mass transport). The equation of state incorporated in the code can handle arbitrary degrees of electron-degeneracy (Nadyozhin 1974a,b; Blinnikov et al. 1996).

The code also includes the effect of the centrifugal force on the stellar structure and chemical mixing and transport of angular momentum due to rotationally induced hydrodynamic instabilities (Heger et al. 2000). The rotational instabilities included are: the Solberg-Høiland instability, dynamical shear instability, secular shear instability, Eddington-Sweet circulation and the Gold-Schubert-Fricke instability. For an extended description of these instabilities and how they are incorporated in the code see Heger et al. (2000).

Chemical mixing and transport of angular momentum due to magnetic effects is also included. The magnetic field is calculated in the following manner: for every timestep, the field is calculated from the angular velocity profile, assuming that it is still winding up due to the differential rotation, but in equilibrium with the magnetic instabilities that reduce the field strength (see Spruit 2002). The magnetic field therefore is instantaneous and has no ‘memory’ of previous models/timesteps. It is a direct result of the differential rotation profile. For more information, see Spruit (2002), Heger et al. (2005), and Petrovic et al. (2005).

Changes of the chemical composition and the nuclear energy generation rate are computed using nuclear networks for the three pp-chains, the four CNO-cycles, the NeNa- and the MgAl-cycle, and the major He, C, Ne and O burning reactions. Also the 3α -reaction is included, and (α,γ) -reactions on ^{12}C , $^{14,15}\text{N}$, $^{16,18}\text{O}$, ^{19}F , $^{20,21,22}\text{Ne}$, and $^{24,25,26}\text{Mg}$. Also (α,n) -reactions on ^{13}C , ^{17}O , $^{21,22}\text{Ne}$, and $^{25,26}\text{Mg}$ and (n,γ) -reactions on ^{12}C , $^{20,21}\text{Ne}$, $^{24,25}\text{Mg}$, and $^{28,29}\text{Si}$. More details are given in Wellstein & Langer (1999) and Wellstein et al. (2001). For all models, OPAL opacities were used (Iglesias & Rogers 1996).

Table 2.1: Overview of the initial models. Throughout this thesis, models can be referred to by their ‘Model Name’: ‘**10N2**’ stands for ‘the non-magnetic $1.0 M_{\odot}$ model with an initial velocity of 2 km/s’. M_i = initial mass, $v_{\text{rot},i}$ = initial velocity.

M_i M_{\odot}	$v_{\text{rot},i}$ km s^{-1}	B-fields? Yes/No	Model Name
1.0	2	No	10N2
1.0	10	No	10N10
1.5	45	No	15N
2.0	140	No	20N
3.0	250	No	30N
1.0	2	Yes	10M2
1.0	10	Yes	10M10
1.5	45	Yes	15M
2.0	140	Yes	20M
3.0	250	Yes	30M

2.2 Initial models

I calculated the evolution of stars starting at the zero-age main sequence for initial masses of 1.0, 1.5, 2.0, and $3.0 M_{\odot}$ with and without the effects of magnetic fields. For all models, a metallicity $Z = 0.02$ was used. The initial equatorial velocities of these models were chosen to be 2, 45, 140, and 250 km s^{-1} , respectively, after Table 1 from McNally (1965) and Fig. 1.1. Since I do not include the effects of magnetic braking, I have chosen the post-magnetic braking velocity of 2 km s^{-1} for the $1.0 M_{\odot}$ model. To study the influence of initial rotation, I also calculated a $1.0 M_{\odot}$ model with an initial velocity of 10 km s^{-1} . I used the Reimers mass loss rate throughout the entire evolution for all models. The choice of stellar wind mass loss rates is important for studies of the late thermally pulsing AGB phase where the wind expels the envelope to leave a white dwarf behind. The total number of thermal pulses in the evolution is also dependant on the mass loss rates. In this study, calculations were pursued for at least five and up to 28 thermal pulses. At this stage the mass loss is so insignificant, that the choice of the AGB mass loss rates does not affect my results significantly.

All parameters and routines not mentioned above are identical to the models from Langer et al. (1999). For an overview of all models, see Table 2.1.

Chapter 3

Angular momentum evolution and white dwarf spins

To study the transport of angular momentum throughout the evolution of my models, I have produced figures that show the integrated angular momentum $J(M_r) = \int_0^{M_r} j(m)dm$, with j the specific angular momentum at mass shell dm , divided by $M_r^{5/3}$, as a function of the mass coordinate M_r . In a rigidly rotating homogeneous sphere, we have $J(M_r)M_r^{-5/3} = \text{const}$. Therefore, finite gradients of $J(M_r)M_r^{-5/3}$ indicate differential rotation. Furthermore, the $J(M_r)$ -profiles from different evolutionary stages trace the flow of angular momentum through the mass shells, since $J(M_r)$ and $J(M_r)M_r^{-5/3}$ remain constant in a given mass shell if no angular momentum is transported through this shell. From this point on, I will refer to plotted data of M_r versus $J(M_r)M_r^{-5/3}$ as $J(M_r)$ -profiles.

For the Hertzsprung-Russel diagram of the magnetic models, see Sect. 6.2 of the Appendix.

3.1 Pre-helium flash

Fig. 3.1 shows $J(M_r)$ -profiles for **10N2** from the zero-age main sequence to right before the helium flash (central density $\sim 10^6 \text{ g cm}^{-3}$). We see that, even though mass is added to the core, the total amount of angular momentum in the core does not grow, since the core edge moves on a line of constant J . The angular velocity profile of the core is shown in Fig. 3.2. We see a kink at $M_r \sim 0.23 M_\odot$. This kink remains at this mass coordinate, although the core grows in mass. The rotational mixing due to the angular velocity gradient at $M_r \sim 0.23 M_\odot$ is obviously not strong enough to smoothen the angular velocity profile. The kink is located at the depth to which the first dredge-up came down, as can be seen in Fig. 3.4. The reason why the total core angular momentum does not grow is shown in Fig. 3.3: all the material that is added has ~ 4 orders of magnitude less specific angular momentum than the inner part of the core. The result is a close to rigidly and fast rotating inner core and a very slow rotating outer core.

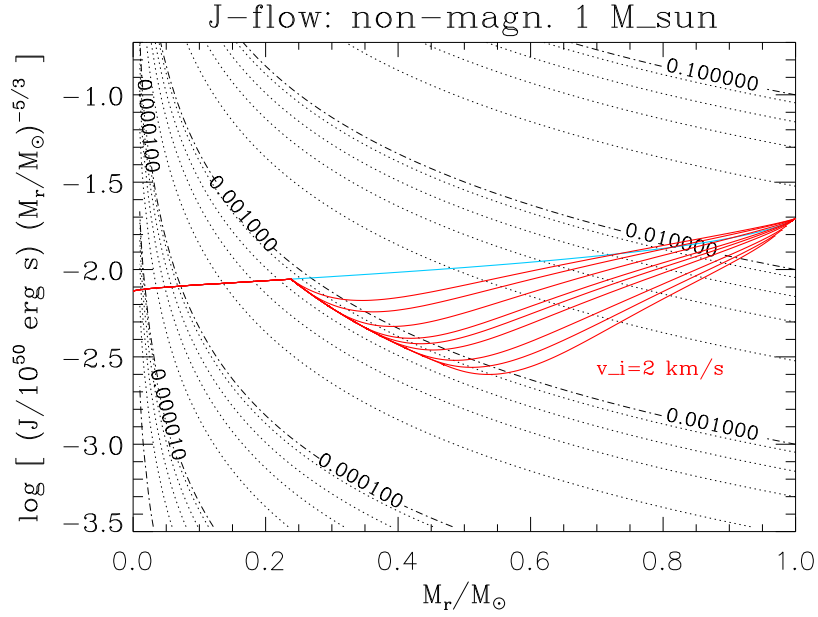


Figure 3.1: $J(M_r)$ -profiles for **10N2**. The contours display levels of constant J , labeled with $\log(J/10^{50}\text{erg s})$. The values for the dotted contours are 3, 5, 7, and 9 times the value of the labeled contour below them. The light blue line is the zero-age main sequence profile. The red lines from top to bottom correspond to the following core densities: $\rho_c = 1 \times 10^5, 2 \times 10^5 \dots 9 \times 10^5 \text{g cm}^{-3}$.

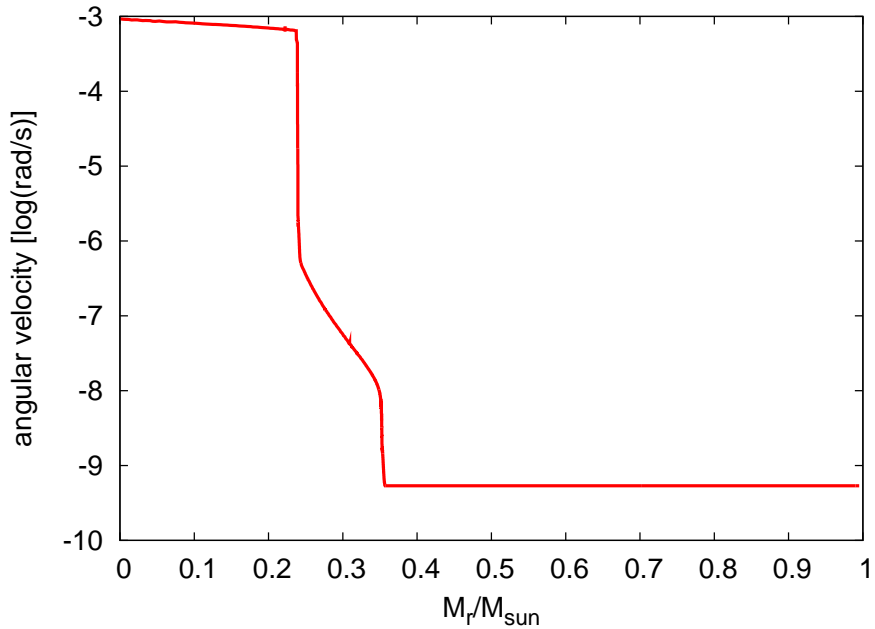


Figure 3.2: Angular velocity profile of **10N2** at $\rho_c = 3 \times 10^5 \text{g cm}^{-3}$, before the helium flash.

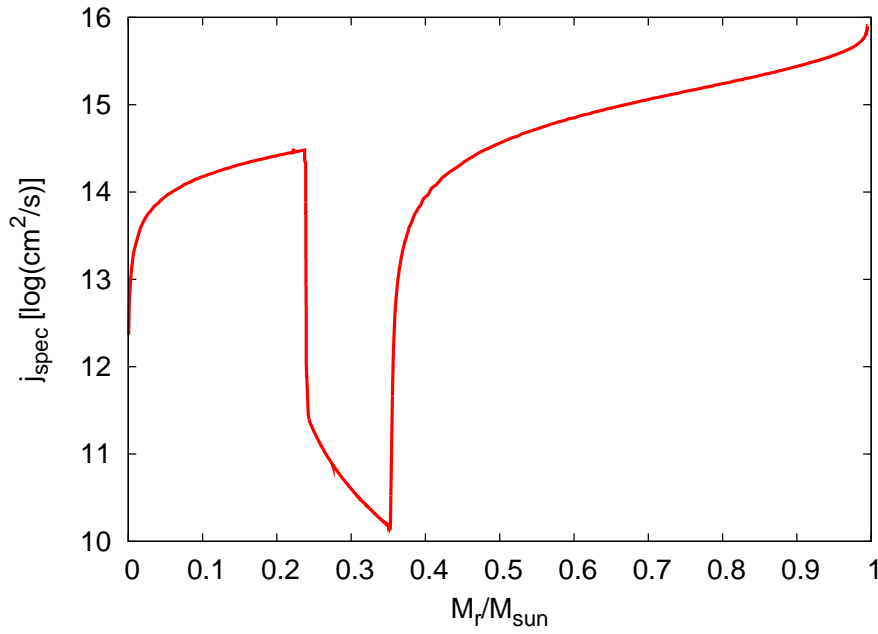


Figure 3.3: Specific angular momentum profile of **10N2** at $\rho_c = 3 \times 10^5 \text{ g cm}^{-3}$, before the helium flash.

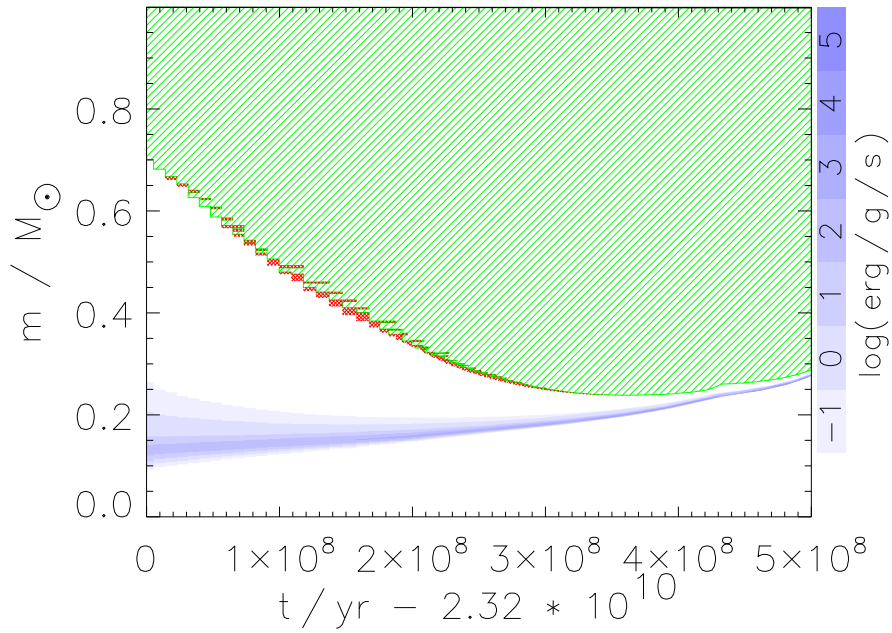


Figure 3.4: Kippenhahn convection plot of **10N2** during the first dredge-up. Green hatched areas are convective. Red signifies semi-convection. The blue shading gives the amount of energy produced by the hydrogen burning shell (see legend).

The angular momentum evolution before the helium flash in the magnetic case, **10M2**, is very different. Fig. 3.5 shows the same part of the evolution as Fig. 3.1, but now for **10M2**. Up to a core density of $\rho_c = 5 \times 10^4 \text{ g cm}^{-3}$, the magnetic fields keep the core rotating rigidly up to the hydrogen burning shell. The core adds angular momentum through the material that is added by the hydrogen burning shell. At a density of $\rho_c = 10^5 \text{ g cm}^{-3}$, we see two little peaks. These correspond to the hydrogen burning shell (left) and the convective envelope (right) that is coming down during the first dredge-up. From this point on we see the hydrogen shell and the convective envelope moving towards each other. At $\rho_c = 2 \times 10^5 \text{ g cm}^{-3}$, the first dredge-up has reached its lowest point and has hereby decided the total core angular momentum. After $\rho_c = 2 \times 10^5 \text{ g cm}^{-3}$, the edge of the core just moves along a line of constant J , which means that after this moment in time, the total amount of angular momentum in the core remains constant. The behaviour of the profiles after $\rho_c = 2 \times 10^5 \text{ g cm}^{-3}$ in Fig. 3.5 remains the same through the first pulses of the thermally pulsing AGB phase, after which the calculations were stopped. This means that there is no angular momentum transport anymore through the mass shells that separate the core from the envelope after the red giant phase.

So, early in the red giant phase, the star's magnetic fields transport angular momentum out of the core which at a core density of $\rho_c = 2 \times 10^5 \text{ g cm}^{-3}$ will not gain or lose any angular momentum any more for the rest of the evolution. The reason why the core does not gain any angular momentum is similar to the **10N2** case. The only material added to the core contains very low angular momentum (a factor ~ 4 lower than the rest of the core, see Fig. 3.6). The magnetic fields keep redistributing the core's angular momentum such that it rotates rigidly (see Fig. 3.7). Since the core grows in mass and adds zero angular momentum material, the mass averaged specific angular momentum of the core will decrease, while the total angular momentum stays constant.

An initial rotation of $v_i = 10 \text{ km/s}$, gives similar results as **10N2**, as we can see in Fig. 3.8. The core is divided in a rigidly rotating center and a slow rotating growing exterior, with the border determined by the first dredge-up. After this, the cores grows and adds zero angular momentum material.

In Fig. 3.9 we see that the magnetic fields in **10M10** are so efficient in removing angular momentum out of the stellar core, that again at $\rho_c = 2 \times 10^5 \text{ g cm}^{-3}$ we have a rigidly rotating core that will not grow in total angular momentum anymore, a similar result as for **10M2**. Fig. 3.10 shows the $J(M_r)$ -profiles of **10M10** and **10M2** together in one plot. We see that from $\rho_c = 2 \times 10^5$ to $9 \times 10^5 \text{ g cm}^{-3}$, the cores of both models converge to almost exactly the same state. Why this happens is unknown at the moment and further studies are necessary (see Chap. 5).

So in all cases discussed above, the first dredge-up determines total core angular momentum and the angular momentum profile from that moment on is such that the cores do not gain angular momentum anymore.

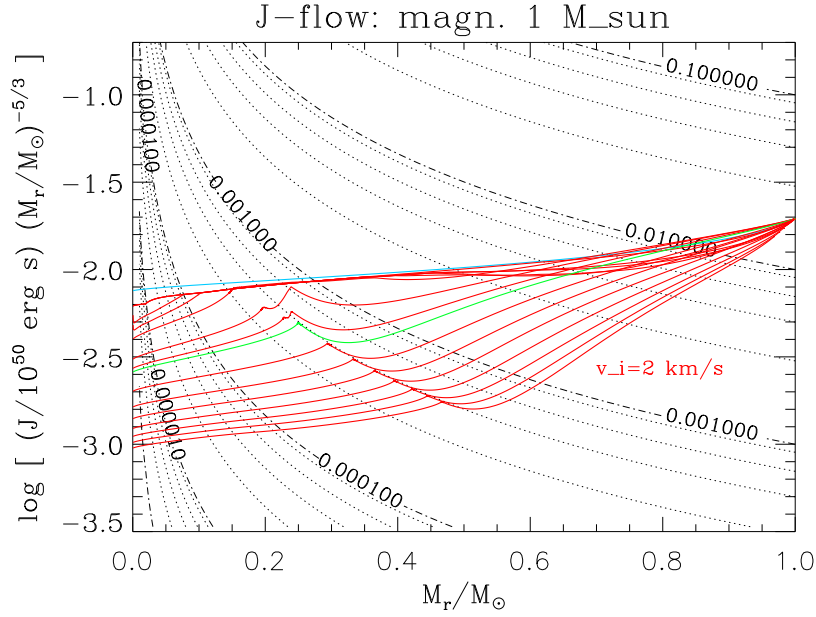


Figure 3.5: $J(M_r)$ -profiles for **10M2**. The contours signify lines of constant J in units of 10^{50} erg s. The light blue line is the zero-age main sequence profile. Consecutive lines from top to bottom correspond to the following core densities: $\rho_c = 10^3, 5 \times 10^3 \dots 10^5, 1.5 \times 10^5 \text{ g cm}^{-3}$. Then the green line corresponds to $\rho_c = 2 \times 10^5 \text{ g cm}^{-3}$ and the lines after that to $\rho_c = 3 \times 10^5 \dots 9 \times 10^5 \text{ g cm}^{-3}$.

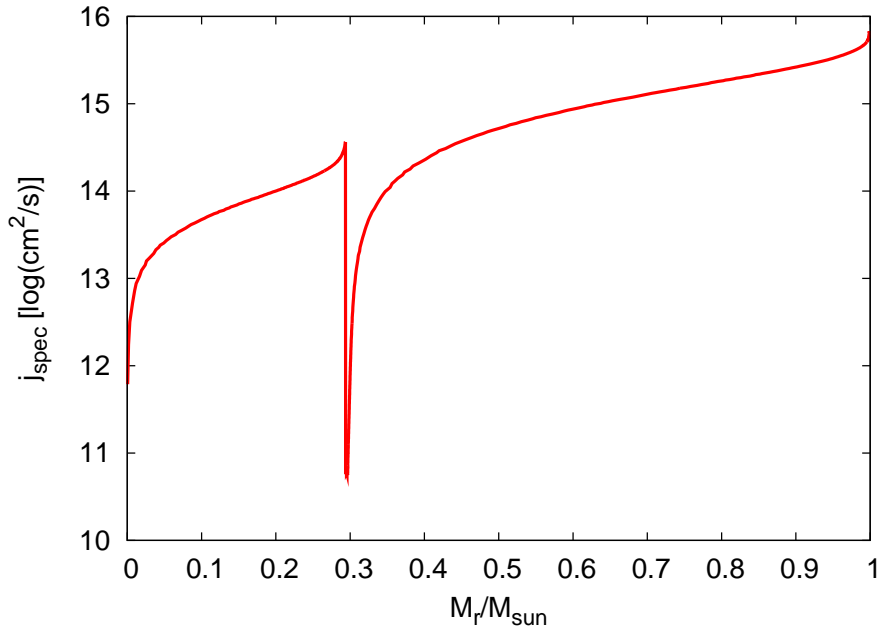


Figure 3.6: Specific angular momentum profile of **10M2** at $\rho_c = 3 \times 10^5 \text{ g cm}^{-3}$, before the helium flash.

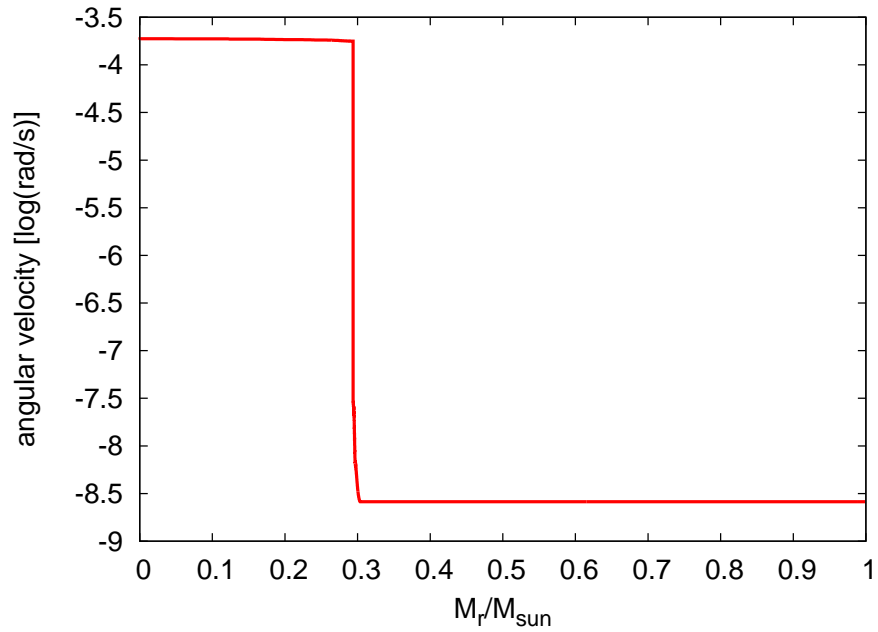


Figure 3.7: Angular velocity profile of **10M2** at $\rho_c = 3 \times 10^5 \text{ g cm}^{-3}$, before the helium flash.

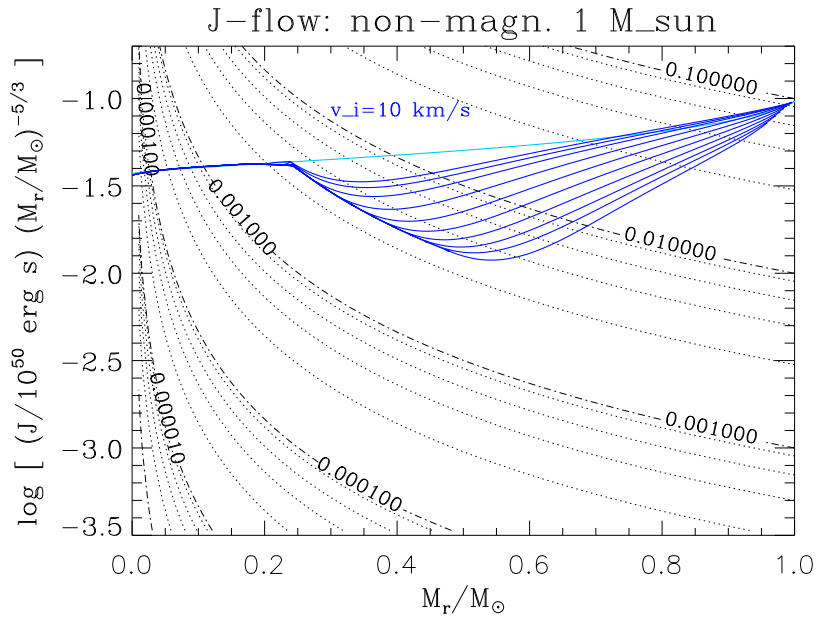


Figure 3.8: $J(M_r)$ -profiles for **10N10**. The contours display levels of constant J , labeled with $\log(J/10^{50} \text{ erg s})$. The values for the dotted contours are 3, 5, 7, and 9 times the value of the labeled contour below them. The light blue line is the zero-age main sequence profile. The red lines from top to bottom correspond to the following core densities: $\rho_c = 1 \times 10^5, 2 \times 10^5 \dots 9 \times 10^5 \text{ g cm}^{-3}$.

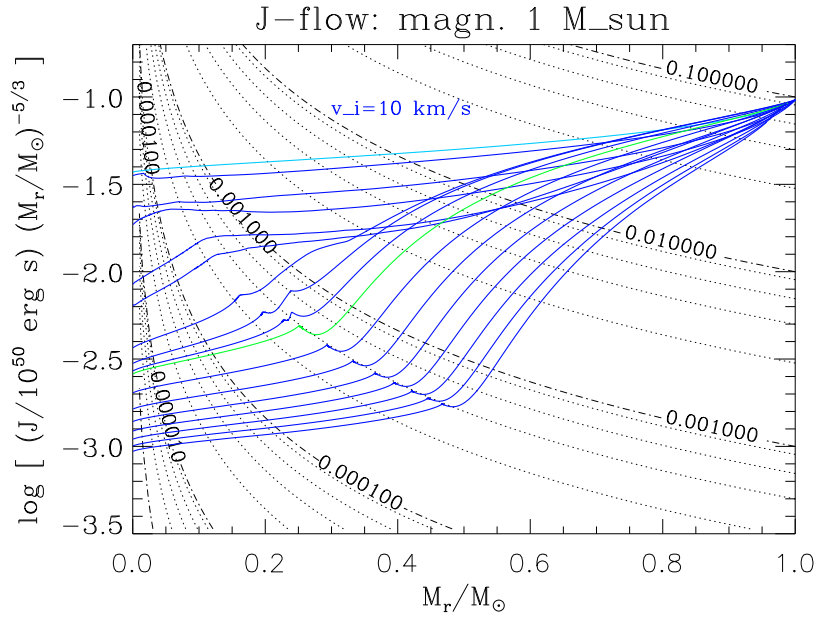


Figure 3.9: Pre-helium flash $J(M_r)$ -profiles of **10M10**. The light blue line is the zero-age main sequence profile. Consecutive lines from top to bottom correspond to the following core densities: $\rho_c = 10^2, 5 \times 10^2 \dots 10^5, 1.5 \times 10^5 \text{ g cm}^{-3}$. Then the green line corresponds to $\rho_c = 2 \times 10^5 \text{ g cm}^{-3}$ and the lines after that to $\rho_c = 3 \times 10^5 \dots 9 \times 10^5 \text{ g cm}^{-3}$.

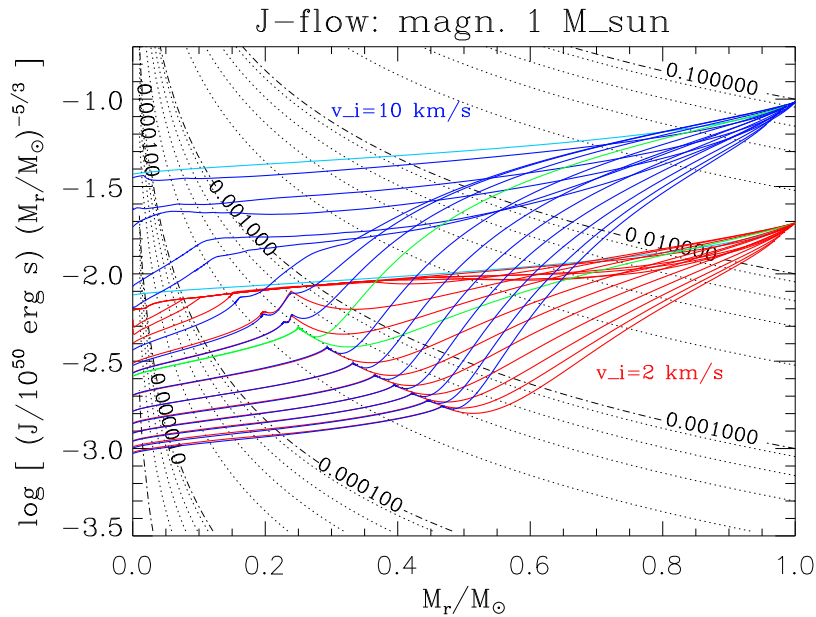


Figure 3.10: Pre-helium flash $J(M_r)$ -profiles of **10M10** and **10M2**.

3.2 From helium flash through AGB/thermally pulsing AGB

Fig. 3.11 shows the helium flash of **10N2**. The helium flash is actually not one single flash, although the first flash is the strongest. It is a repetitive convective burning flash that ‘eats’ its way down to the core. When the core is reached, steady core helium burning starts.

These consecutive convective flashes redistribute the angular momentum in the core in my non-magnetic models, as shown in Figs. 3.12 and 3.13. The ‘kink’ present in the angular velocity profile is hereby removed by the helium flashes. The total angular momentum in the core, however, does not change during this process.

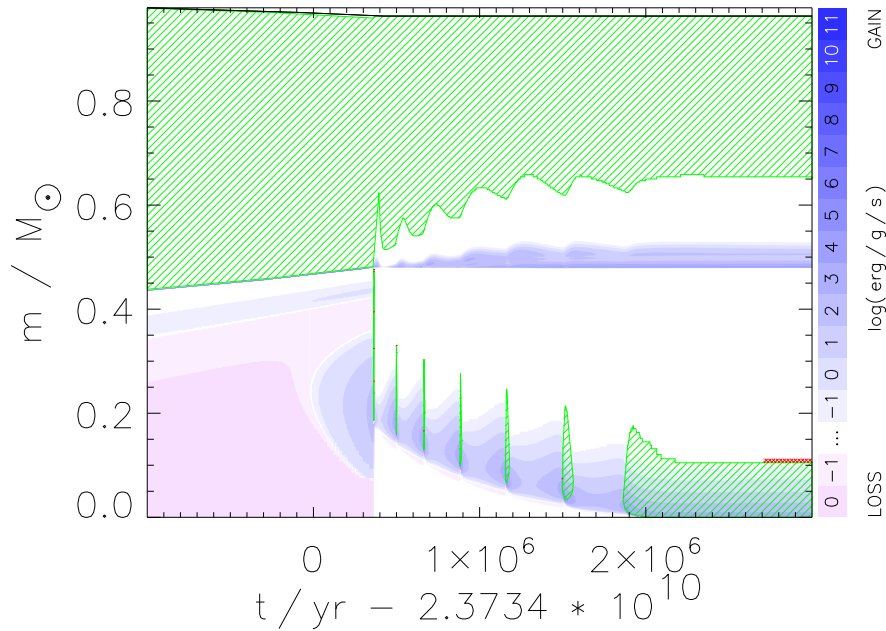


Figure 3.11: The helium flash of **10M2**. Green hatching is convection. Red is semi-convection. Pink shading signifies energy loss due to neutrino-emissions, blue hatching signifies energy production due to nuclear burning (see legend).

The total amount of angular momentum in the cores of my magnetic models does not change anymore during and after the helium flash. Zero angular momentum material will still be added and the magnetic fields keep redistributing the angular momentum in the cores to maintain rigid rotation.

Fig. 3.14 shows the flow of angular momentum of **15N** and **15M**. It is clear that the magnetic fields slow the cores down before core helium burning. Total core angular momentum remains constant up to the first part of the thermally pulsing AGB phase, where the calculations were stopped. The results for the $1.0 M_{\odot}$ and $2.0 M_{\odot}$ models are similar. In the $3.0 M_{\odot}$ case, the transport of angular momentum out of the stellar cores stops later, during the helium burning phase. At the end of the core helium burning phase, however, total core angular

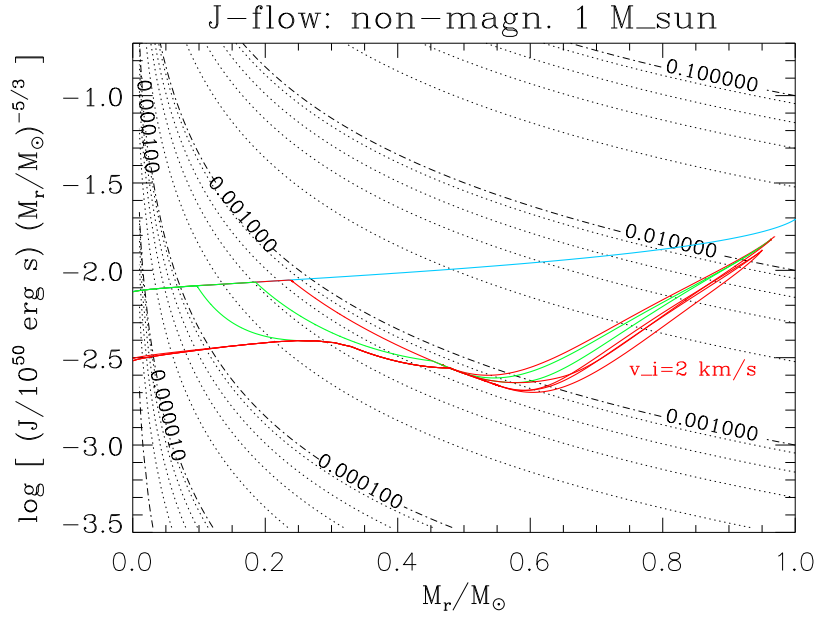


Figure 3.12: $J(M_R)$ -profiles of **10N2**. The light blue line is the zero-age main sequence. The upper red line is pre-helium flash. The green lines are during the helium flash and the lower red lines are all post-helium flash.

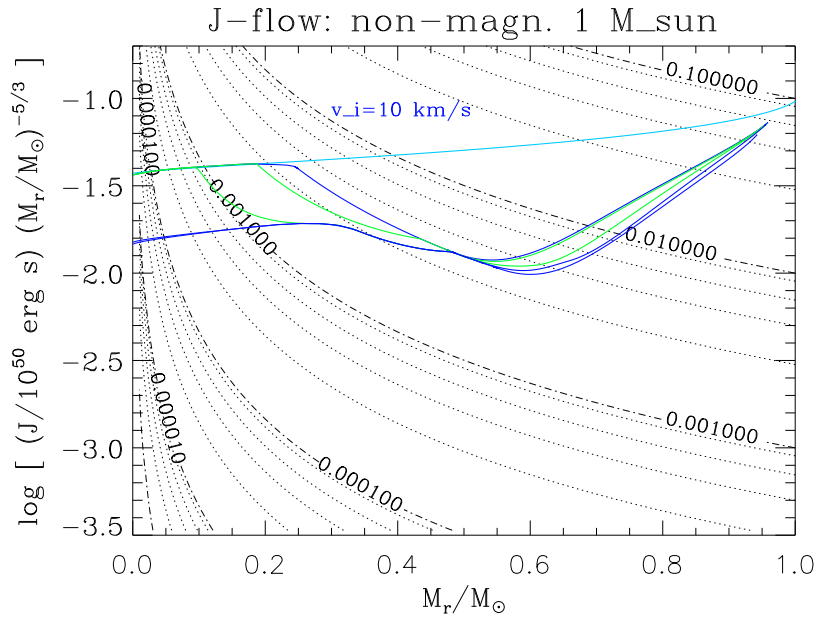


Figure 3.13: $J(M_R)$ -profiles of **10N10**. The light blue line is the zero-age main sequence. The upper dark blue line is pre-helium flash. The green lines are during the helium flash and the lower dark blue lines are all post-helium flash.

momentum remains constant.

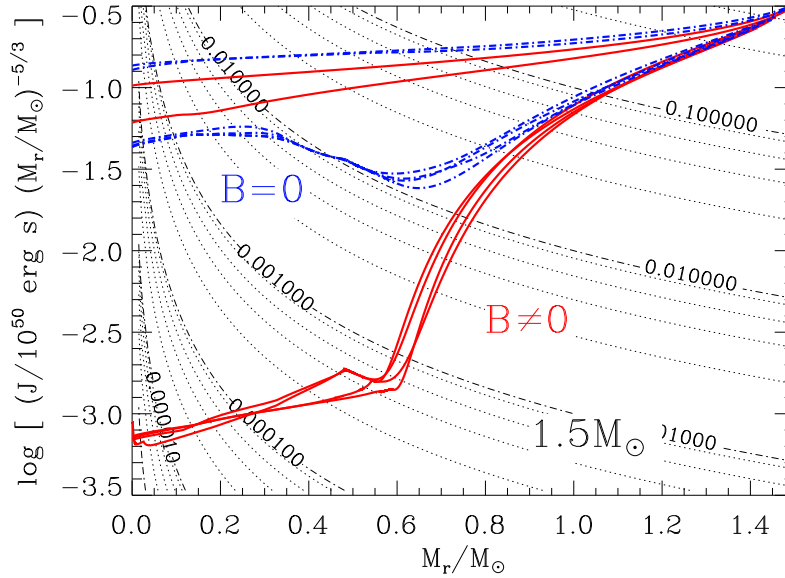


Figure 3.14: $J(M_R)$ -profiles of **15N** and **15M**. From high to low the six lines per model represent the following evolutionary stages: start main sequence ($X_c = 0.7$), main sequence ($X_c \sim 0.25$), start core helium burning ($X_c \sim 0$), helium burning ($Y_c \sim 0.4$), start thermally pulsing phase and during thermally pulsing phase (>4 pulses).

In any case, total core angular momentum remains constant at least after the core helium burning phase. The final $J(M_r)$ -profiles during the thermally pulsing AGB phase of all models, except for **10N10** and **10M10**, are plotted in Fig. 3.15.

3.3 White dwarf spins

Since the total angular momentum of the core of all models does not change anymore from early red giant stage all the way through the first five or more thermal pulses, I assume that it will stay constant throughout the rest of the evolution, even to the white dwarf stage. The core is fully decoupled from the outer layers of the star and there is no reason to assume that it will get coupled later on. Fig. 3.16 shows that the cores are already on the cooling track towards white dwarf stage: they will lose their envelopes, shrink and cool down.

With the assumption made above, I can estimate white dwarf rotational velocities. I calculated these velocities using the gyration radii, H , for polytropes derived by (Motz 1952):

The angular velocity of the white dwarf (assumed to be a rigidly rotating polytrope with polytropic index $n = 1.5$, a mass M_{wd} and total angular momentum J_{tot}) is equal to the angular velocity of a point mass (mass M_{wd} and angular

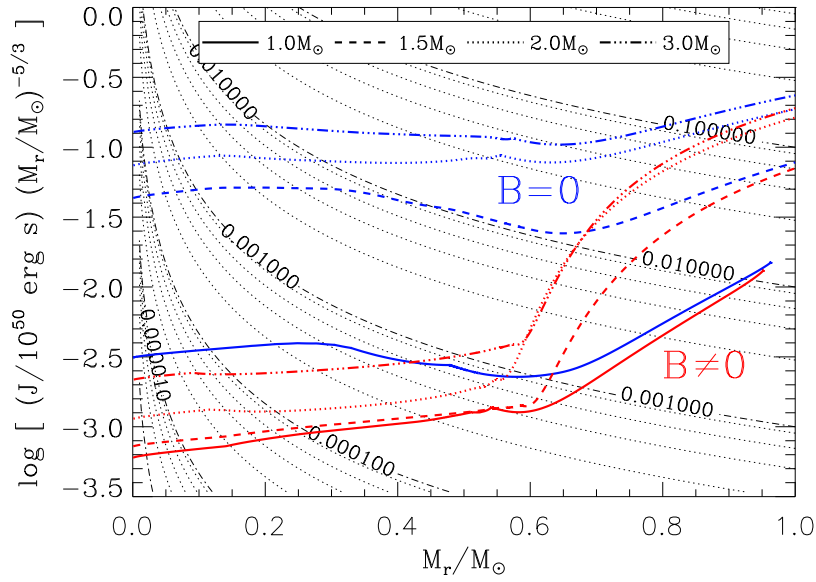


Figure 3.15: Final $J(M_R)$ -profiles for models **10N2&10M2**, **15N&15M**, **20N&20M**, and **30N&30M**.

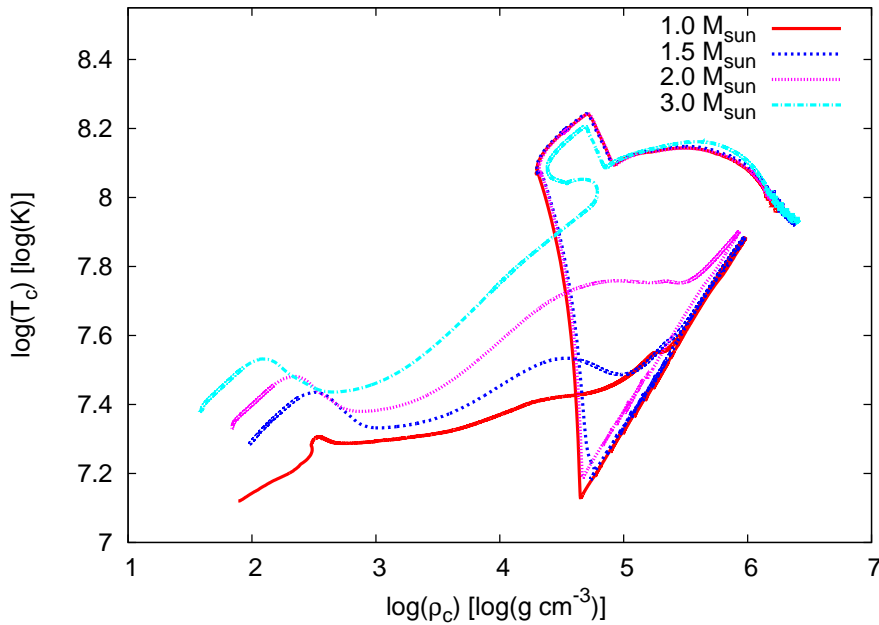


Figure 3.16: Central density (ρ_c) versus central temperature (T_c) of the evolution of **10M2**, **15M**, **20M**, **30M**.

momentum J_{tot}) if the point mass rotates at radius H , where H and the radius of the white dwarf R_{wd} obey the following relation (Table 1 in Motz (1952)):

$$\left(\frac{H}{R_{\text{wd}}}\right)^2 = 0.20502 \quad (3.1)$$

Since the point mass and the white dwarf have the same angular momentum and the same angular velocity, their moments of inertia I are also equal ($\omega = J/I$):

$$I_{\text{wd}} = H^2 M_{\text{wd}} \quad (3.2)$$

Now we find for the surface velocity $v_{\text{rot,wd}}$:

$$v_{\text{rot,wd}} = \omega_{\text{wd}} R_{\text{wd}} = \frac{J_{\text{tot}}}{I_{\text{wd}}} R_{\text{wd}} = \frac{J_{\text{tot}}}{0.20502 R_{\text{wd}} M_{\text{wd}}}, \quad (3.3)$$

with ω_{wd} the angular velocity of the white dwarf, M_{wd} the predicted mass of the white dwarf from initial-final mass relations from Weidemann (2000) and R_{wd} the predicted radius of the white dwarf from mass-radius relations from Hamada & Salpeter (1961).

These calculated velocities and other values for all models are listed in Table 3.1. Fig. 3.17 shows the mass averaged specific angular momentum for all models and the observational limit of $\sim 10 \text{ km s}^{-1}$ (converted to mass averaged specific angular momentum) from Berger et al. (2005). Also plotted are values for neutron stars from models calculated by Heger et al. (2005). We see that the models that start out as rapid main sequence rotators (mass $\gtrsim 1.2 M_{\odot}$) all produce white dwarfs that rotate faster than the upper limit by Berger et al. (2005) when magnetic effects are not included. **10N2** started out with a post-magnetic braking value, and lies under the upper limit.

Heger et al. (2005) compared $15 M_{\odot}$ models with and without magnetic fields and found similar results for their neutron stars. Observational limits for neutron star rotation rates favoured their magnetic models. This is a similar result as in my low mass study and illustrates that magnetic fields have a large influence on the angular momentum distribution in stars of with $1 M_{\odot} \lesssim M_{\star} \lesssim 15 M_{\odot}$ if not *all* masses.

M_i M_\odot	$v_{\text{rot},i}$ km s^{-1}	TP #	M_{wd} M_\odot	R_{wd} $10^{-2} R_\odot$	$J_{c,f}/10^{46}$ $\text{g cm}^2 \text{s}^{-1}$	$j_{c,f}/10^{13}$ $\text{cm}^2 \text{s}^{-1}$	ω_{wd} s^{-1}	$v_{\text{rot},\text{wd}}$ km s^{-1}
1.0M	2	3	0.550	1.25	4.94	4.49	0.00031	2.6
1.0M	10	5	0.550	1.25	5.01	4.54	0.00031	2.6
1.5M	45	8	0.575	1.20	5.83	5.07	0.00038	3.0
2.0M	140	6	0.600	1.19	8.05	6.71	0.00057	4.5
3.0M	250	24	0.680	1.08	15.4	11.3	0.0013	9.1
1.0	2	0	0.550	1.25	8.07	7.33	0.00040	4.2
1.0	10	4	0.550	1.25	39.5	35.9	0.0025	21
1.5	45	11	0.575	1.20	110	95.6	0.0070	56
2.0	140	4	0.600	1.19	329	274	0.023	180
3.0	250	28	0.680	1.08	458	336	0.031	220

Table 3.1: Initial mass (M_i) (M signifies presence of magnetic fields), initial equatorial velocity ($v_{\text{rot},i}$), total number of calculated thermal pulses TP, assumed white dwarf mass (M_{wd}) from Weidemann (2000), assumed white dwarf radius (R_{wd}) from Hamada & Salpeter (1961), final total angular momentum (J_{tot}), final mass averaged specific angular momentum $j_{c,f} = J_{c,f}/M_{\text{wd}}$, estimated white dwarf angular velocity (ω_{wd}) and estimated equatorial velocity ($v_{\text{rot},\text{wd}}$) from Eq. 3.3.

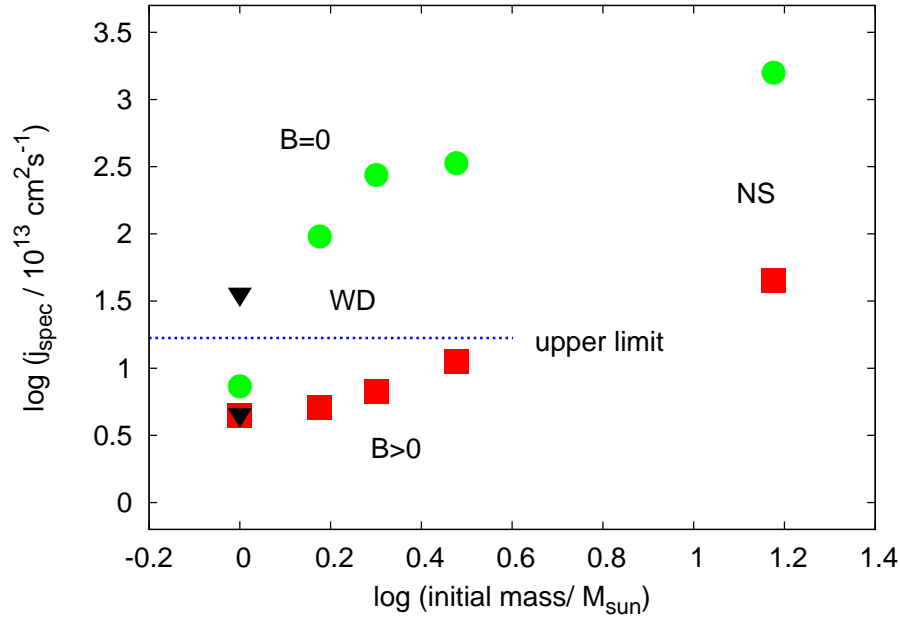


Figure 3.17: Initial mass versus mass averaged specific angular momentum of all models (see Table 3.1). Green circles are non-magnetic models, red squares are magnetic. The upper black triangle is **10N10** and the lower black triangle is **10M10**. The blue dotted line shows the observational upper limit from Berger et al. (2005). The two far right models with initial mass = $15 M_\odot$ show data for neutron stars from Heger et al. (2005).

Chapter 4

Chemical mixing

4.1 Early evolutionary phases

The surface abundances of low mass stars during the main sequence can only change if there is a chemical mixing process that can transport nuclear burning products all the way up to the surface. Convection mixes layers as well, but on the main sequence, these stars do not have a convective envelope yet. When the convective envelope is formed during the first dredge-up, elements from the hydrogen burning reactions are brought up to the surface. After this, surface abundances will change during the second dredge-up and during the third dredge-ups of the thermally pulsing AGB phase.

This means that if the surface abundances of hydrogen burning products change before the first dredge-up, rotational mixing must be strong enough to accomplish this. Figs. 4.1 and 4.2 show the surface abundance evolution of CNO-elements in **30N** and **30M**. It is clear that the CNO-abundances change before the first dredge-up and hence rotational mixing has a big influence on the chemical composition and profile of these stars.

4.2 AGB/TP-AGB phase

All my models showed a very weak third dredge-up. In none of my models did the dredge-up reach below the original position of the hydrogen burning shell. This means none of my models had a proton-rich layer touching a ^{12}C -rich layer. The typical situation for the helium shell flash and third dredge-up is shown in Fig. 4.4. The third dredge-up does not come down below the hydrogen shell position and the flash does not come very close to the hydrogen shell position. I tried to produce a deeper third dredge-up by decreasing the sensitivity to mean molecular weight barrier. I also modified the reaction rates for the triple alpha reaction and CNO-cycle to get a stronger helium shell flash. Both attempts did not produce a deeper dredge-up. Why these methods did not work and how a stronger dredge-up should be obtained is still unclear. Further studies are necessary (see Chap. 5).

In **30N**, however, the rotational mixing was strong enough to bring some ^{12}C and protons together to form a ^{13}C -pocket and a neighbouring ^{14}N -pocket. These two layers were fully mixed by the strong rotational mixing (as happened

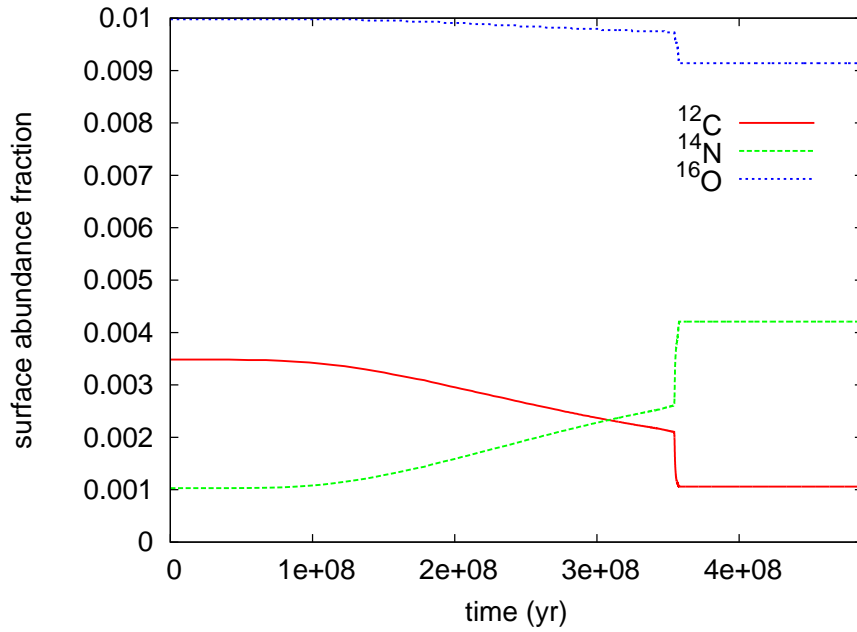


Figure 4.1: Surface abundance evolution of CNO-elements of **30N**. The first dredge-up happens at $t \sim 3.5 \times 10^8$ yr.

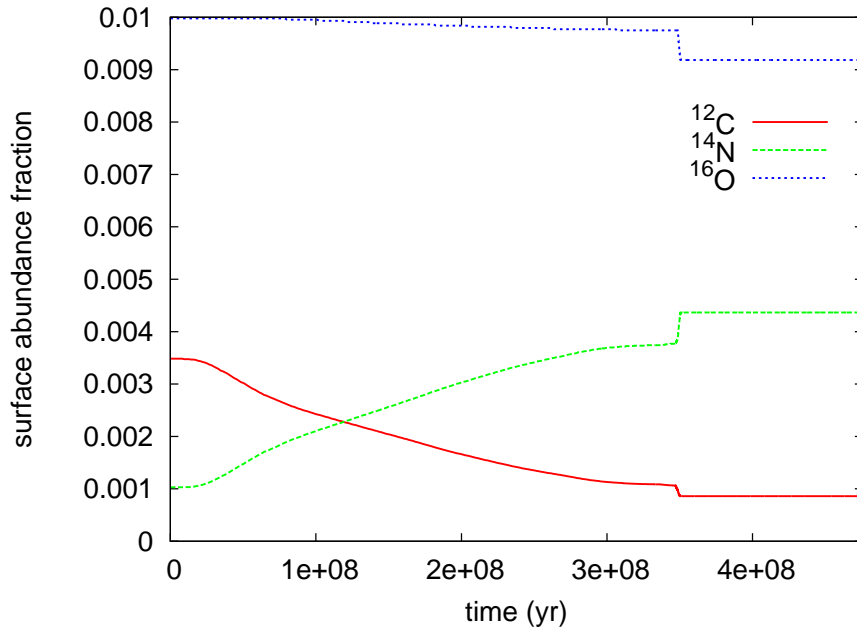


Figure 4.2: Surface abundance evolution of CNO-elements of **30M**. The first dredge-up happens at $t \sim 3.5 \times 10^8$ yr.

in the models by Herwig et al. (2003) and Siess et al. (2004)). The resulting abundance profiles are shown in Fig. 4.3.

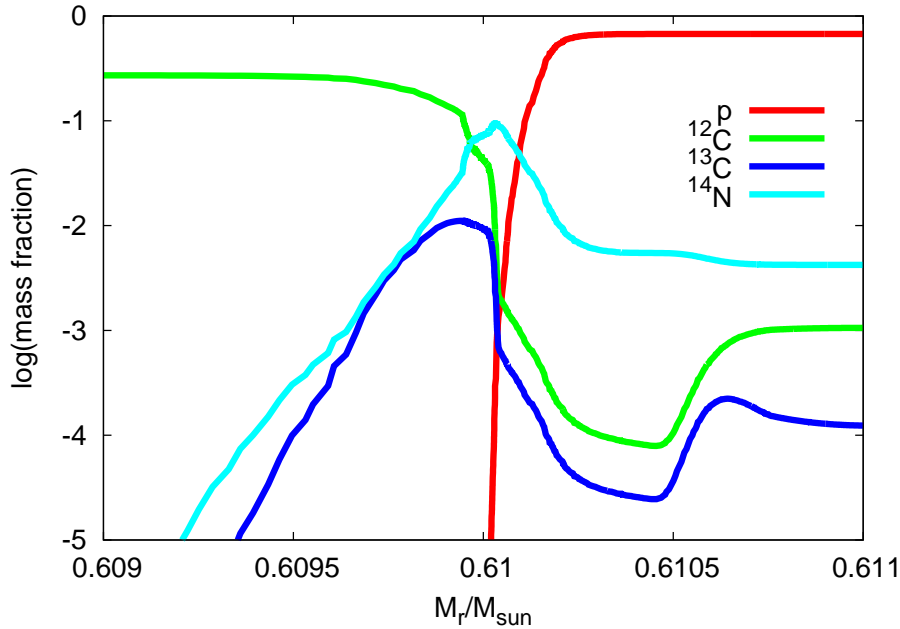


Figure 4.3: ^{13}C -pocket engulfed with ^{14}N during the interpulse phase of **30N**. The red line shows the protons brought down by the third dredge-up. The green line shows the ^{12}C formed by the helium shell flash. The dark blue and the light blue line show the ^{13}C and the ^{14}N , respectively, formed by the mixing of protons and ^{12}C .

Although no ^{13}C -pockets are formed in my magnetic models, an analysis of the diffusion coefficients in my models is still relevant. Even without a dredge-up, a significant reduction (a factor of $\sim 10^2$ according to Herwig et al. (2003)) of the diffusion coefficients would be a promising result.

Figs. 4.5 and 4.6 show a Kippenhahn convection diagram of the same thermal pulses of models **30N** and **30M**. It is obvious that the magnetic models possess less rotational mixing. Fig. 4.7 and 4.8 show that the magnetic fields are able to bring the diffusion coefficients down by a factor of $\sim 10^3$ in the relevant layers. The relevant layers ('s-process region') are the layers between the helium and hydrogen shell sources, in these models $M_r \approx 0.545 \dots 0.565$. If a factor of 10^3 still provides enough mixing to even *form* a ^{13}C -pocket, is not clear. Further studies must provide an answer to this question.

Models **20N** and **20M** show a decrease in diffusion coefficients by a factor of $\sim 10^2$ in the s-process region, as shown in Fig. 4.9.

The same comparison for models **15N** and **15M** shows a factor of $\sim 10^2$ difference in the amount of rotational mixing, as shown in Fig. 4.10, although the absolute values for the diffusion coefficient are so low that a ^{13}C -pocket might not be formed at all.

Models **10N2** and **10M2** (see Fig. 4.11) have low diffusion coefficients. In the middle of the s-process region, the non-magnetic model has orders of magni-

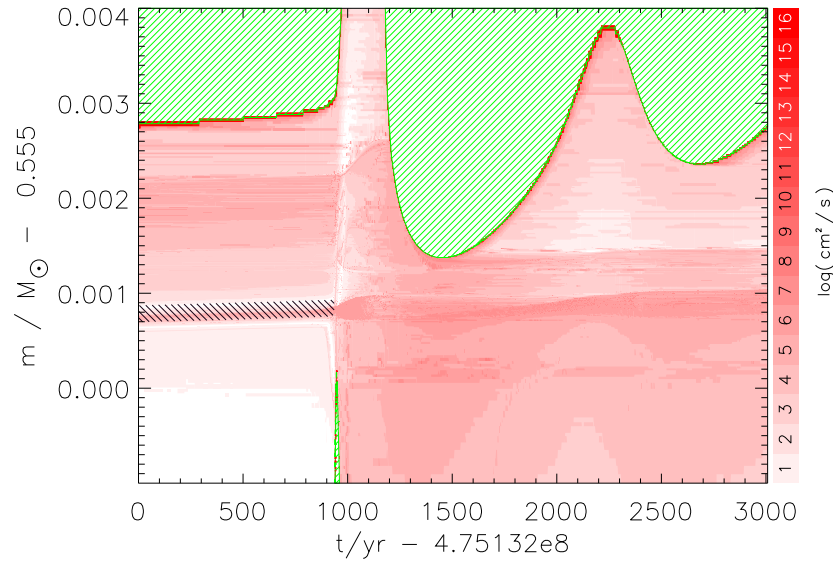


Figure 4.4: Kippenhahn diagram of the third dredge-up and helium shell flash of thermal pulse #5 of **30M**. The green hatching corresponds to areas of convection and red spots on the edge of the convective areas indicate semi-convection. The black hatching is the hydrogen burning shell. The red shading shows the values for the diffusion coefficients due to rotational mixing (see legend).

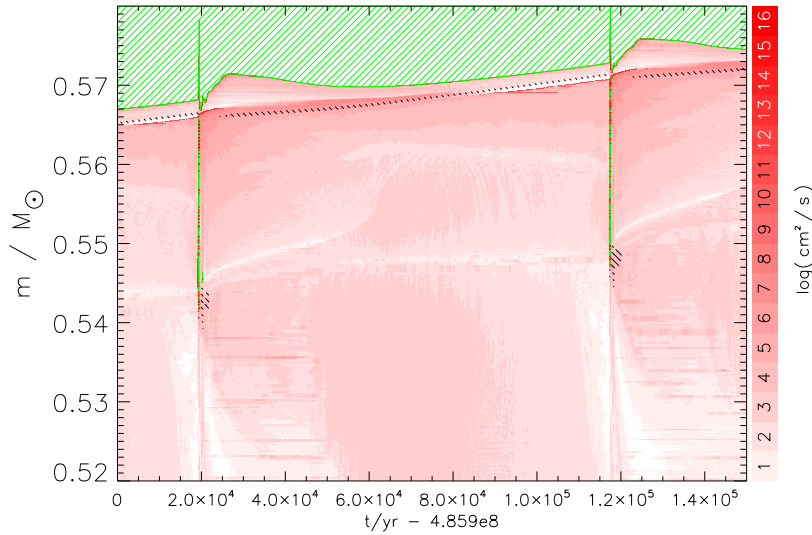


Figure 4.5: Kippenhahn diagram of thermal pulse #7 and #8 of **30N**. The green hatching corresponds to areas of convection. The black hatching is the hydrogen burning shell. The red shading shows the values for the diffusion coefficients due to rotational mixing (see legend).

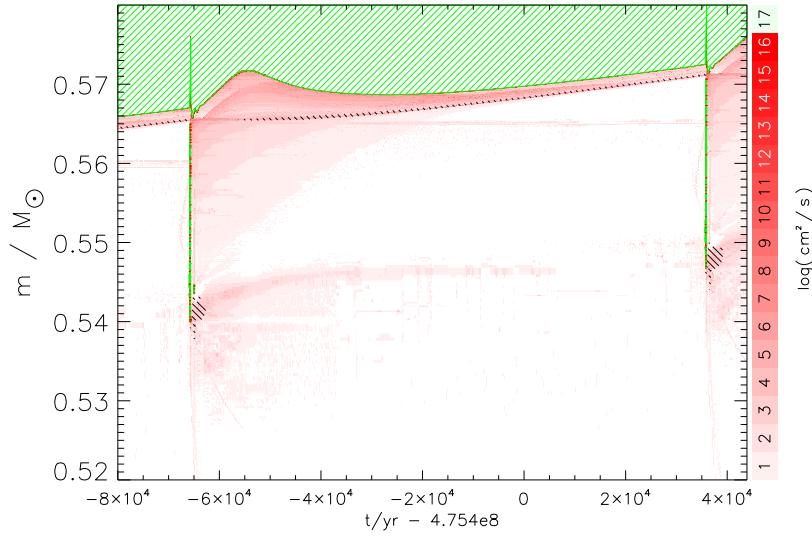


Figure 4.6: Kippenhahn diagram of thermal pulse #7 and #8 of **30M**. The green hatching corresponds to areas of convection. The black hatching is the hydrogen burning shell. The red shading shows the values for the diffusion coefficients due to rotational mixing (see legend).

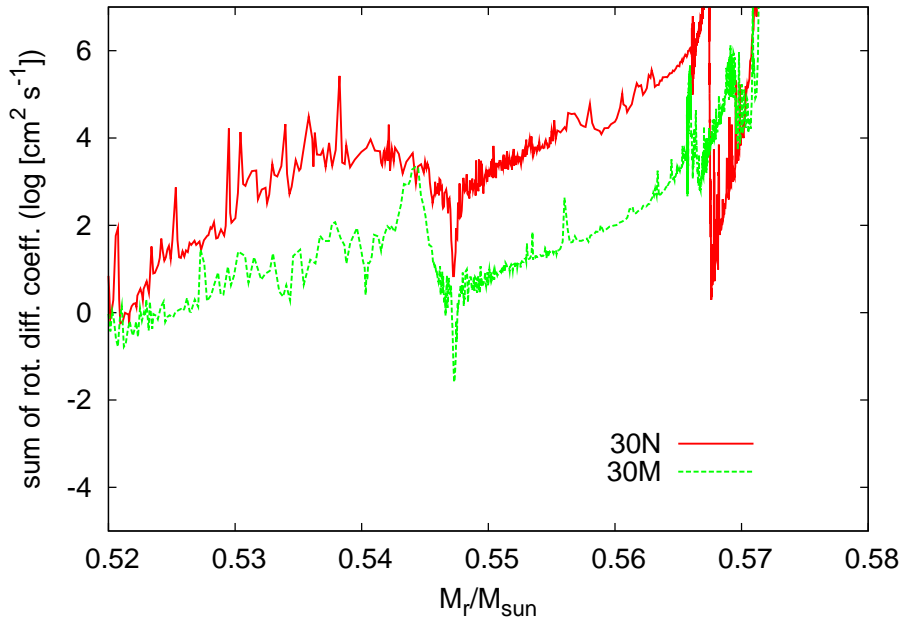


Figure 4.7: Diffusion coefficients ~ 10000 yrs after thermal pulse #7 of **30N** and **30M**. The s-process region ranges from $M_r \approx 0.545 \dots 0.565$.

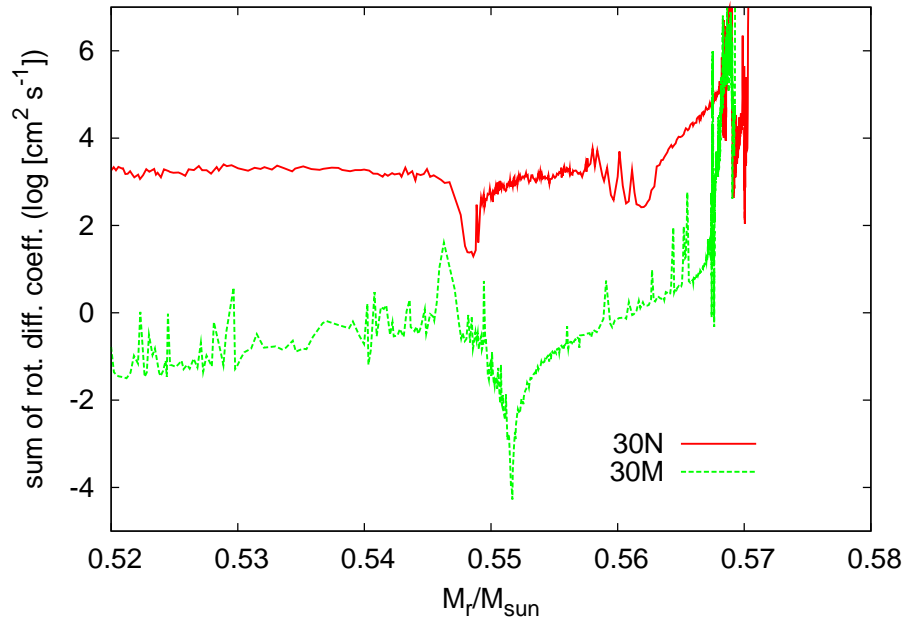


Figure 4.8: Diffusion coefficients ~ 40000 yrs after thermal pulse #7 of **30N** and **30M**. The s-process region ranges from $M_r \approx 0.545 \dots 0.565$.

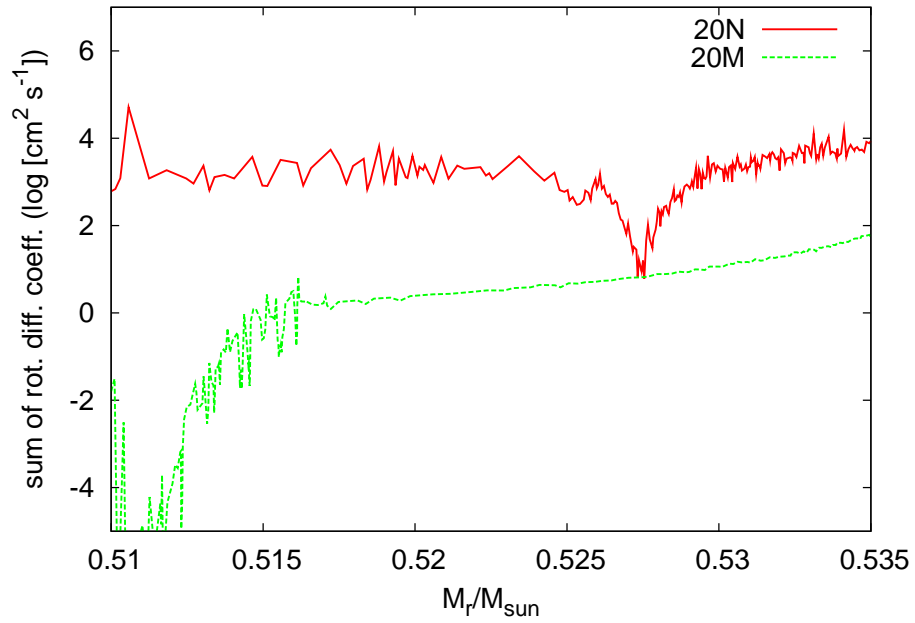


Figure 4.9: Diffusion coefficients ~ 10000 yrs after thermal pulse #4 of **20N** and **20M**. The mass range corresponds to the s-process region.

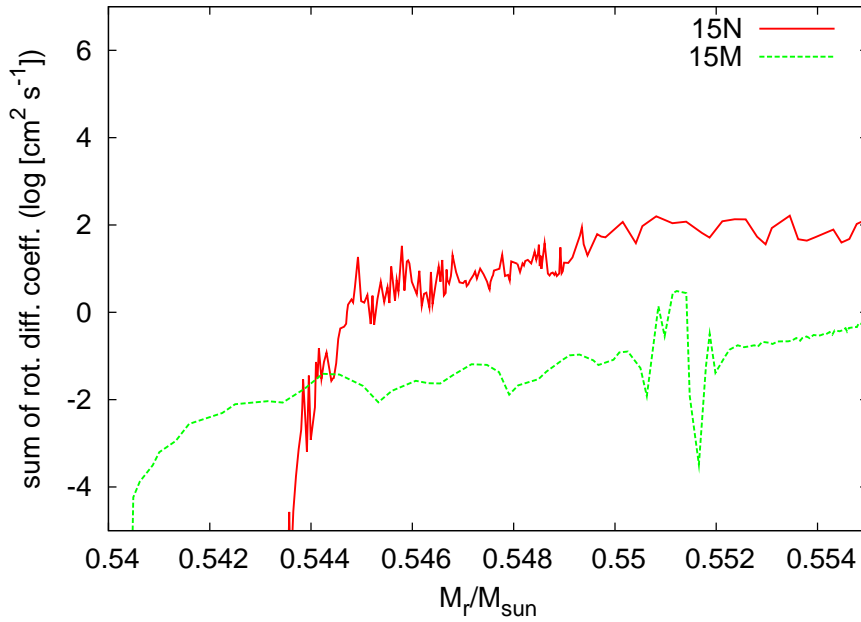


Figure 4.10: Diffusion coefficients ~ 10000 yrs after thermal pulse #5 of **15N** and **15M**. The mass range corresponds to the s-process region.

tude lower diffusion coefficients than the magnetic model. Close to the hydrogen burning shell, the diffusion coefficients are similar and close to the helium burning shell, the diffusion coefficients of the magnetic model are orders of magnitude higher than the non-magnetic model. Both models show layers with no mixing at all (diffusion coefficients $< 10^{-4}$). The only mixing can occur through layers with $M_r \gtrsim 0.539$.

All magnetic models (except the $1.0 M_{\odot}$ case) show a significant reduction of the diffusion coefficients in the region where the s-process should take place. The question if the obtained reduction factors of $10^2 - 10^3$ really produce a stable ^{13}C -pocket can only be answered if models with a deeper third dredge-up are obtained. More research has to provide these models.

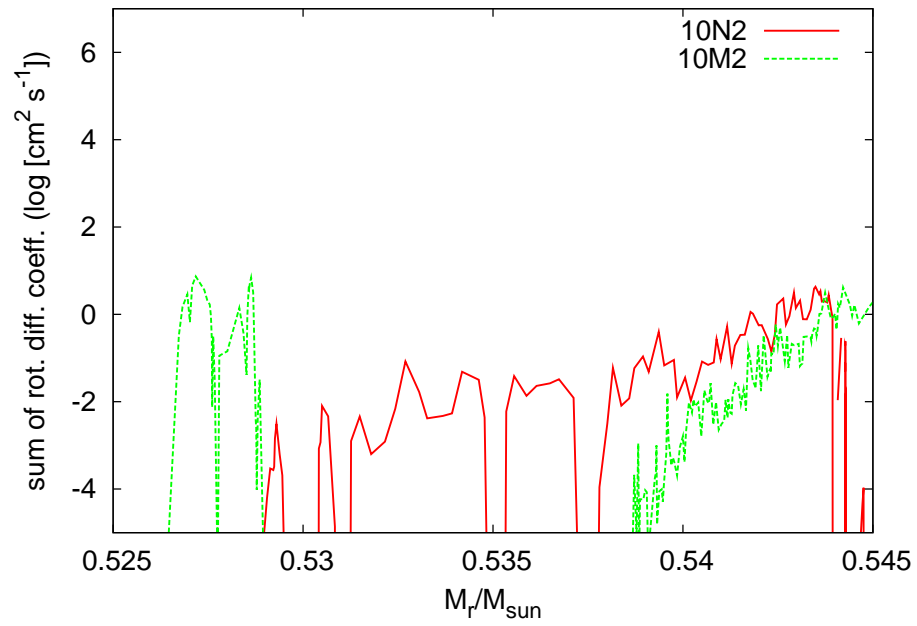


Figure 4.11: Diffusion coefficients ~ 10000 yrs after thermal pulse #4 of **10N2** and **10M2**. The mass range corresponds to the s-process region.

Chapter 5

Summary and outlook

I found that magnetic fields are able to remove a considerable amount of angular momentum from the stellar cores of models before the core helium flash. So much even, that the magnetic models without magnetic braking now produce white dwarfs with spins below the recent observational upper limit by Berger et al. (2005), while their non-magnetic counterparts produce white dwarfs with velocities up to ~ 20 times the upper limit. The influence of rotationally induced instabilities is insignificant in the $1 M_{\odot}$ model.

Since magnetic fields have such a big influence on the angular momentum evolution of these stars (and of $\sim 15 M_{\odot}$ stars according to Heger et al. (2005), I conclude that they are an essential addition to the physics to be considered in stellar models of *all* masses.

Why the final state of the stellar cores in **10M2** and **10M10** is so similar is still far from understood. More research has to be done on this matter.

I have also found that magnetic fields reduce the amount of rotational mixing by factors of 10^2 to 10^3 for my magnetic models with masses of $1.5 \dots 3.0 M_{\odot}$. The question if a ^{14}N -free ^{13}C -pocket can be formed under these mixing conditions cannot be answered directly from my models, since the third dredge-ups obtained in all magnetic models are so weak that no ^{13}C or ^{14}N is even formed. However, I can conclude that the reduction due to the magnetic fields of the diffusion coefficients is very promising.

Further studies have to be done to get a stronger third dredge-up in models of $1.0 \dots 3.0 M_{\odot}$ to be able to answer the question if magnetic fields can really produce a suitable s-process environment.

Chapter 6

Appendix

6.1 What are thermal pulses and the third dredge up?

When low mass stars have burned up all the helium in the core and the helium burning shell is formed, the stars will climb up the asymptotic giant branch again in the Hertzsprung-Russel diagram (see A in Fig. 6.1). At this point in the evolution the helium burning shell will become so thin that it becomes unstable.

This instability manifests itself in the following way: if the pressure/temperature in the shell goes up a little, the shell will increase in luminosity and will expand, but since it is so extremely thin, even a large factor of expansion will not push the star's envelope up enough to let the pressure/temperature go down, which causes the luminosity of the helium shell to grow even more, especially since helium burning is extremely temperature sensitive. In this way the shell's luminosity grows with a very large factor before the shell is actually big enough to push up the envelope and therefore cool down. When the shell finally manages to push the outer layers of the star up, the following happens:

1. The hydrogen burning shell cools down so rapidly because of the expansion of the envelope that it extinguishes.
2. The size and luminosity of the helium burning shell increase extremely for a very short moment (a few years). The shell convectively burns helium almost up to the hydrogen burning shell and therefore forms ^{12}C all the way up there¹. This is called a helium shell flash - not to be confused with the helium flash that ignites core helium burning earlier on in the evolution.
3. The convective envelope of the star comes down. This effect is called third dredge-up (3DU). The strength of the 3DU depends on numerous factors, for example: core mass, chemical barriers the 3DU encounters on its way down and the strength of the helium flash. In the case of a strong 3DU, it reaches down further than the original position of the extinguished

¹The timescale on which mixing in convective layers occurs is so short compared to the other relevant timescales, that we can consider chemical mixing in convective layers instantaneous.

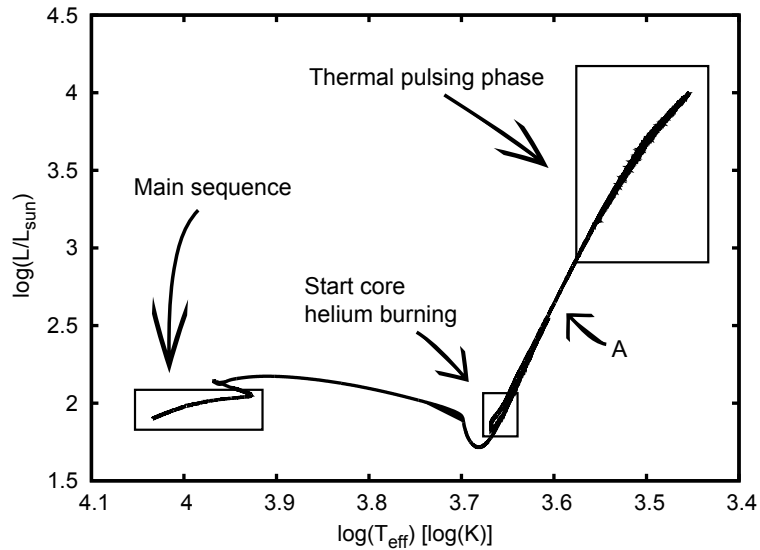


Figure 6.1: Hertzsprung-Russel diagram of a magnetic $3 M_{\odot}$ model.

hydrogen burning shell, mixing hydrogen (free protons) from the envelope into these layers. In this case we have a layer with protons that touches a layer with ^{12}C .

4. The helium shell cools due to the expansion of the star and therefore shrinks.
5. The star decreases in radius, because of the absence of hydrogen burning, and therefore the pressure in the star goes up.
6. The pressure/temperature are high enough for the hydrogen shell to ignite again.
7. The helium shell becomes so thin that it becomes unstable again and the next thermal pulse occurs. The phase between two consecutive pulses is called the interpulse phase.

This repetitive pulsing process in which the star moves up and down on the AGB (see Fig. 6.1) keeps going on until the strong stellar winds have expelled the envelope of the star. What is left is a CO white dwarf. For an overview of a thermal pulse and flash in a Kippenhahn diagram, see Fig. 6.2.

6.2 Hertzsprung-Russel diagram

Fig. 6.3 displays the Hertzsprung-Russel diagram of all magnetic models. **10M2** and **10M10** overlap.

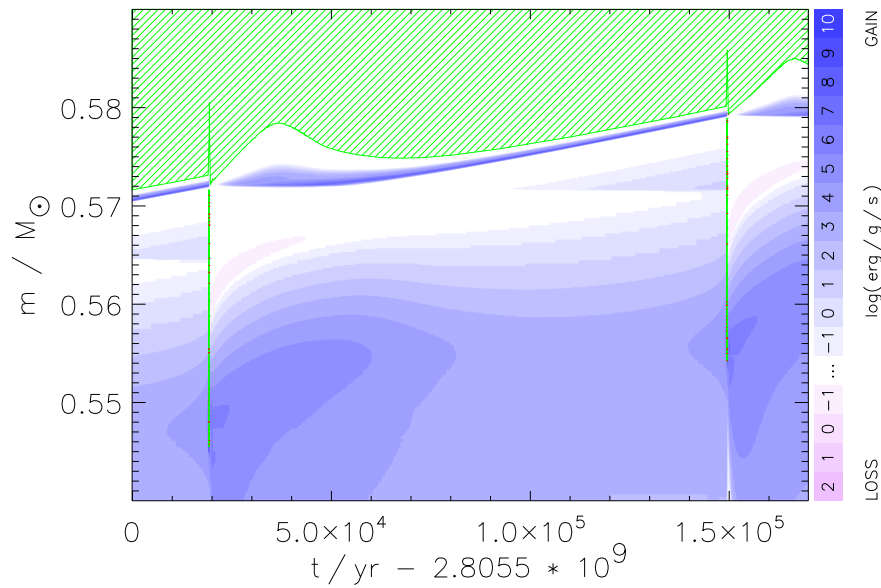


Figure 6.2: Kippenhahn convection diagram of a thermal pulse and interpulse phase to the next pulse. The green hatching signifies convection, the blue shading signifies energy generation due to nuclear burning (see legend) and the pink shading signifies energy loss due to neutrino-emissions.

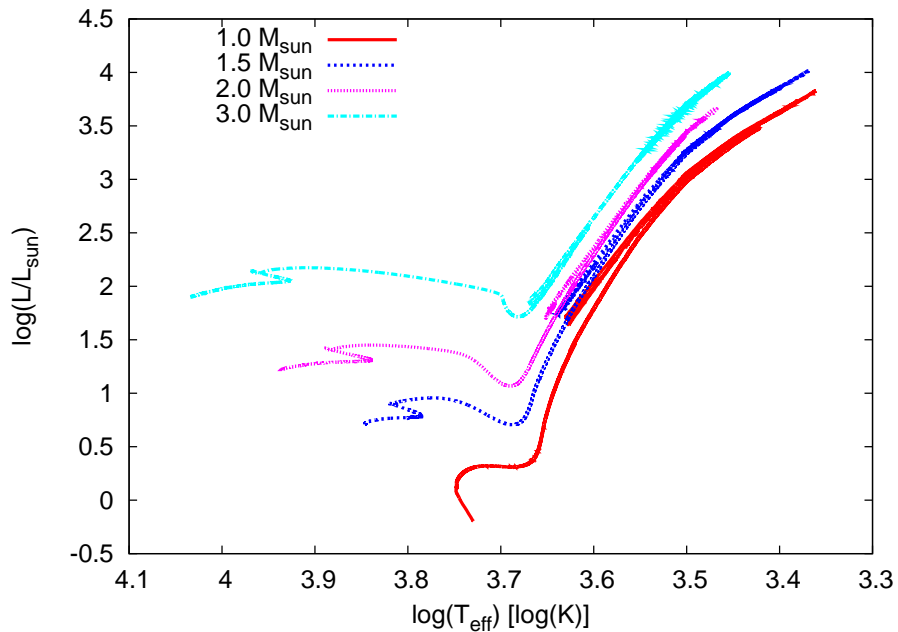


Figure 6.3: Hertzsprung-Russel diagram of all magnetic models.

Bibliography

- Abia, C., Domínguez, I., Gallino, R., et al. 2003, Publications of the Astronomical Society of Australia, 20, 314
- Berger, L., Koester, D., Napiwotzki, R., Reid, I. N., & Zuckerman, B. 2005, **A&A**, 444, 565
- Blinnikov, S. I., Dunina-Barkovskaya, N. V., & Nadyozhin, D. K. 1996, **ApJS**, 106, 171
- Eggenberger, P., Maeder, A., & Meynet, G. 2005, **A&A**, 440, L9
- Hamada, T. & Salpeter, E. E. 1961, **ApJ**, 134, 683
- Heger, A., Langer, N., & Woosley, S. E. 2000, **ApJ**, 528, 368
- Heger, A., Woosley, S. E., & Spruit, H. C. 2005, **ApJ**, 626, 350
- Herwig, F. 2005, **RAA**, 43, 435
- Herwig, F., Langer, N., & Lugaro, M. 2003, **ApJ**, 593, 1056
- Iglesias, C. A. & Rogers, F. J. 1996, **ApJ**, 464, 943
- Lambert, D. L. 1989, in IAU Colloq. 106: Evolution of Peculiar Red Giant Stars, ed. H. R. Johnson & B. Zuckerman, 101–130
- Langer, N., Heger, A., Wellstein, S., & Herwig, F. 1999, **A&A**, 346, L37
- McNally, D. 1965, The Observatory, 85, 166
- Motz, L. 1952, **ApJ**, 115, 562
- Nadyozhin, D. K. 1974a, Nauchnye Informatsii, 32, 3
- Nadyozhin, D. K. 1974b, Nauchnye Informatsii, 33, 117
- Palacios, A., Talon, S., Charbonnel, C., & Forestini, M. 2003, **A&A**, 399, 603
- Petrovic, J., Langer, N., Yoon, S.-C., & Heger, A. 2005, **A&A**, 435, 247
- Siess, L., Goriely, S., & Langer, N. 2004, **A&A**, 415, 1089
- Spruit, H. C. 2002, **A&A**, 381, 923
- Stauffer, J. R. 2003, in IAU Symposium 215: Stellar rotation, ed. A. Maeder & P. Eenens, 127–135

Stępień, K. 1988, **ApJ**, 335, 907

Talon, S. & Charbonnel, C. 2005, **A&A**, 440, 981

Weidemann, V. 2000, **A&A**, 363, 647

Wellstein, S. & Langer, N. 1999, in ASP Conf. Ser. 173: Stellar Structure: Theory and Test of Convective Energy Transport, 189

Wellstein, S., Langer, N., & Braun, H. 2001, **A&A**, 369, 939

Acknowledgements

First of all, I thank my **parents** for always choosing what was best for me when I was young and for always supporting me with whatever I wanted to do later in life. They are the best parents I could ever wish for. I've rarely seen people who would sacrifice and have sacrifices so much for the well-being of their children.

Then, I want to thank my supervisor **Norbert Langer** for all his help and clear explanations. I appreciate the way he never tried to put pressure on me, even though I wasn't around as much as he might have hoped for. I have great respect for him.

Also I would like to thank **Falk Herwig** and **Alexander Heger** for the fruitful and insightful discussions we had on their respective trips to Utrecht, **Sung-Chul Yoon** for all his technical help and **Arend Jan Poelarends**, who always took the time to help me with any problems I came across during my research.

Finally, I thank my sister **Annelies** and my girlfriend **Kate** who never ever stopped believing in me.